nature biotechnology

Supplementary information

https://doi.org/10.1038/s41587-026-03158-5

Optically detected and radio wave-controlled spin chemistry in flavoproteins

In the format provided by the authors and unedited

Supplementary Information

Supplementary Note 1. Reference experiments

We observe a negative magnetic field effect, that is, a reduction in PL intensity upon application of a magnetic field in our *Cra*Cry data. This contrasts with previous studies involving a different class of cryptochromes[1] (e.g., *At*Cry). Although the underlying reasons are not yet understood, we currently attribute this difference to experimental conditions (e.g., optical excitation power) which may cause the formation of alternative SCRPs. Future work will further investigate these findings.

In order to exclude the influence of free FAD in solution, which is known to cause a negative MFE, we performed additional experiments[1,2]. Each experiment was performed with a fresh thawed sample of *Cra*Cry, to avoid degradation effects, UV/Vis spectra were recorded for checking the protein state, which show characteristic features of an intact protein (Fig. S1a). The most prominent features of bound FAD are a slight red shift of the absorption maximum from 445 to 450 nm and the three-peak pattern of this absorption maximum[3,4], both of which are clearly observed in our samples. Degradation of the protein and escape of the flavin to the solution is clearly observed after long measurements (which we avoided). We purposely exposed *Cra*Cry to 37° for 16 hours and observed that the ODMR signal disappeared, which proves that an intact protein is needed for efficient ODMR (Fig. S1b). For that reason, we always used fresh samples for our experiments.

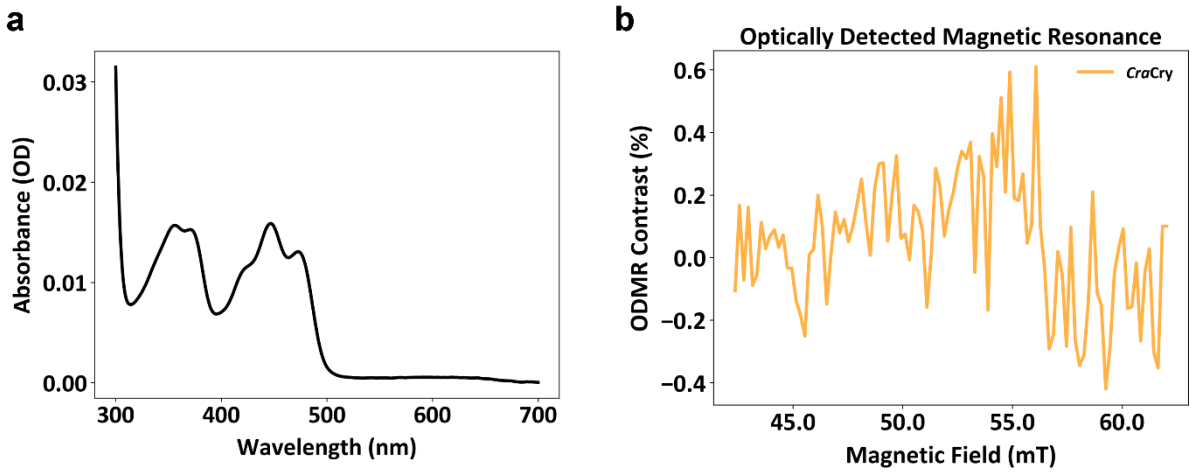

Figure S1. Characterization of thermal stability of *Cra*Cry. a) Protein sample directly taken from - 80 °C and prepared as described in the sample preparation section for ODMR and MFE measurements. b) Incubation at 37 °C for 16 hours results in a complete loss of ODMR contrast.

Supplementary Note 2. Lineshape modulation induced by the RF delivery

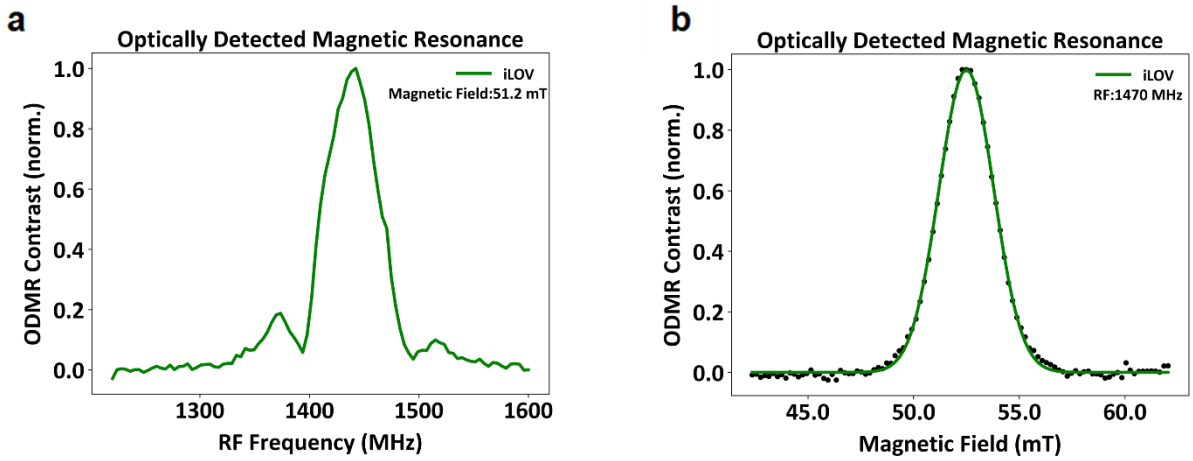

Figure S2. Artifacts induced by the power dependency of the RF delivery. a) An RF sweep at a static magnetic field shows a spectroscopic signature, which disappears when the magnetic field is swept under constant RF drive (b).

In Figure S2a, when the RF is swept at a fixed magnetic field, the signal exhibits multiple peaks, which we attribute to uneven power delivery across the frequency band. To avoid this artifact, the RF is fixed, and the magnetic field is swept (Fig. S2b). This configuration reveals a single peak, which is well-described by a Gaussian fit.

Supplementary Note 3. Magnetic field strength calibration with boron nitride nanotubes (BNNTs)

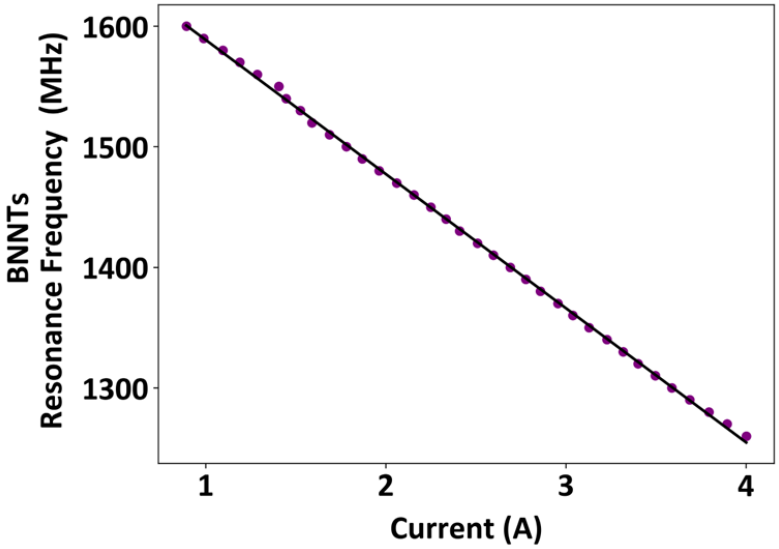

Figure S3. Calibration of the current to magnetic field using ODMR of BNNTs.

The calibration of the magnetic field strength was performed using boron nitride nanotubes (BNNTs) purchased from NanoIntegris Inc. which have been characterized before[5,6]. The BNNTs have an average diameter of ~50 nm and lengths of a few micrometers. As-received BNNT powder was dispersed in 0.25% Triton X-100, stirred on a plate for 4 hours, followed by 10 minutes of sonication. Afterwards, the BNNT suspension was applied to a glass coverslip in a laminar flow hood, allowing solution to evaporate and fix BNNTs on the coverslip. The

laser power was adjusted to 500 µW to excite the BNNTs and PL was collected using a 647 nm long pass filter (647 LP Edge Basic Longpass Filter, Semrock).
The calibration was performed by sweeping the current for the copper coils from 1 to 4 A while fixing the RF at 35 distinct values, spaced evenly between 1250-1600 MHz. At each frequency, we recorded an ODMR spectrum of the BNNTs. Fitting each spectrum with a Gaussian function yielded the current for the resonance frequency. This procedure established a direct calibration curve between applied current and magnetic field strength.

Supplementary Note 4. Optimizing ODMR contrast of iLOV

To optimize the ODMR contrast, the RF was set to 1256 MHz, the point of maximum contrast at 45 mT. The PL was recorded over 100 steps (10 ms exposure each) and the laser intensity was fixed at ~5.9 µW µm^{-2}. Figure S4a depicts PL counts versus number of frames for “RF on” and “RF off”. Here, the readout time t constitutes a time trace of the PL intensity evolution, where each step represents a 10 ms time point. In addition to the bleaching kinetics, the RF field produces a significant enhancement of PL intensity. Analysis of the “RF on” / “RF off” PL ratio (offset corrected) in Figure S4b reveals a steady increase in ODMR contrast as a function of readout time. These results indicate that the optimal ODMR contrast is obtained with the following sequence: simultaneous laser and RF excitation, followed by a delayed PLreadout which terminates synchronously with the laser turning off.

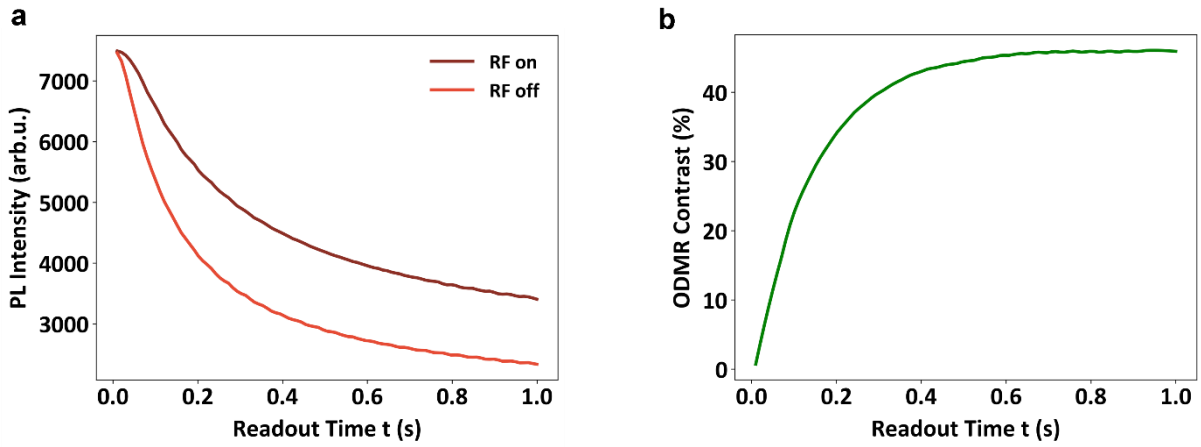

Figure S4. PL intensity as a function of the readout time t (each step corresponds to 10 ms). a) Raw data. b) ODMR contrast.

The second factor for optimizing ODMR contrast is laser intensity (see also Fig. S5). For this measurement, laser intensity was adjusted from ~ 0.1 to 5.9 µW µm^{-2} (30 linear steps) and the exposure time was 500 ms. Each time a total of two frames were acquired, where the signal from the second frame was used for the analysis due to the larger contrast. Figure S5a demonstrates that the RF-induced PL change increases with laser intensity. This is further quantified in Figure S5b by plotting the offset-corrected ODMR contrast (“RF on” / “RF off”). We attribute this to the fact that a higher laser intensity accelerates the photochemical cycle of iLOV, allowing the system to reach the photochemical equilibrium faster.

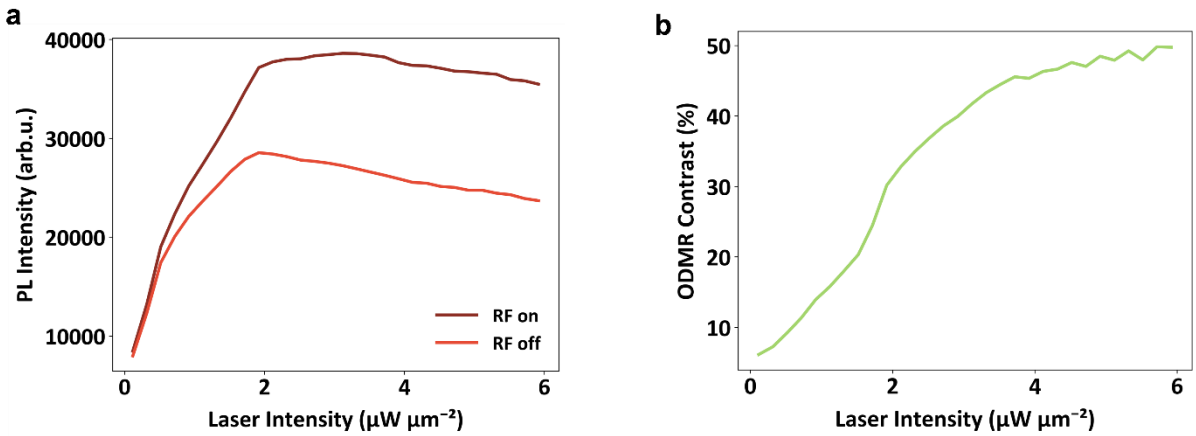

Figure S5. PL intensity as a function of laser intensity. a) Raw data. b) ODMR contrast.

These experiments demonstrate how RF and optical excitation (among other factors) affect the underlying chemical equilibrium of the spin chemistry.

Supplementary Note 5. Stability and robustness of iLOV

To assess thermal stability, iLOV was kept at 37 °C for 16 hours. Subsequent ODMR measurements revealed no signal degradation, confirming iLOV's superior thermal stability. We also performed experiments with the same sample over days at room temperature with only very minor degradation of the ODMR properties. To rule out a potential solvent effect, notably the glycerol concentration, on the ODMR linewidth, iLOV was measured in the *Cra*Cry buffer (50 mM NaH_2PO_4 pH 7.8, 100 mM NaCl, 50% (v/v) glycerol). The result shows no significant change in linewidth, confirming that the observed spectral differences are intrinsic to the proteins and not an artifact of the solvent environment (Fig. S6b)

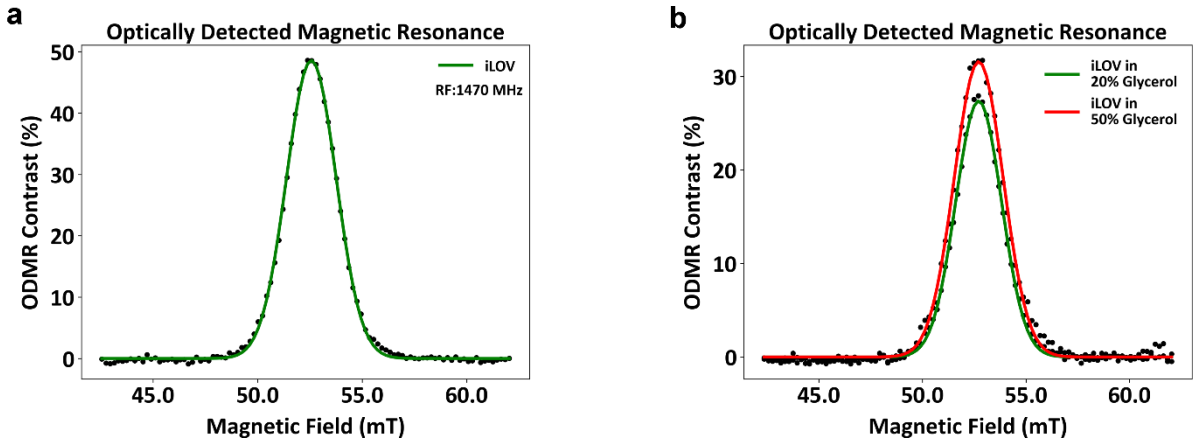

Figure S6. iLOV ODMR after heating the sample at 37 °C (a) for 16 hours and after exchange to a phosphate-based buffer system with higher glycerol concentration (b).

Supplementary Note 6. Linewidth and ODMR power-dependency analysis for iLOV

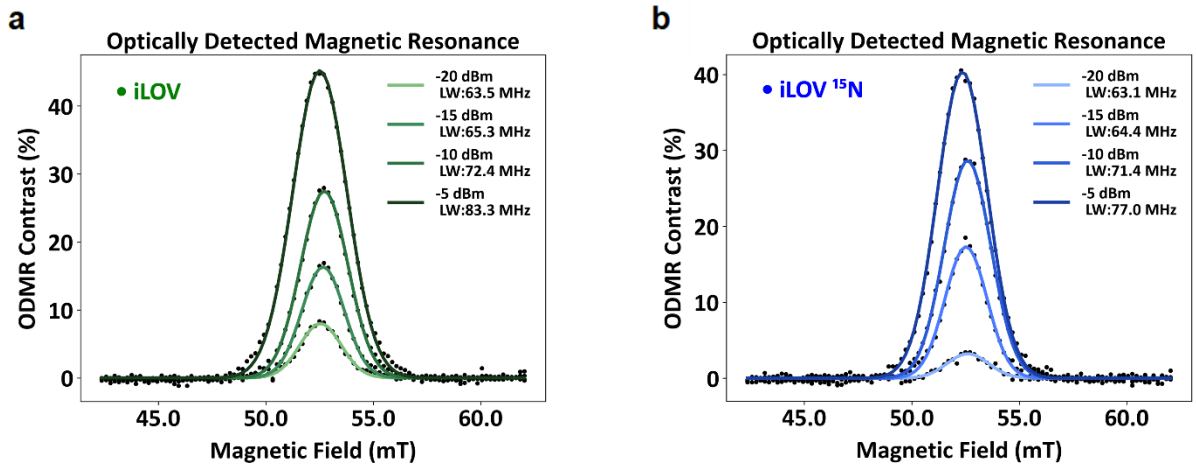

Figure S7. ODMR signal as a function of RF power. The power values refer to the output power of the signal source and do not reflect the actual power at the sample position. a) iLOV ODMR signal as a function of RF power. b) Uniformly labeled ^{15}N iLOV ODMR signal as a function of RF power.

To avoid artifacts from RF-power broadening, we performed linewidth measurements as a function of the applied RF power in conjunction with ^{15}N-labelling of iLOV (Fig. S7). We cannot determine the exact RF power at the sample position; therefore, we report the output power of our signal generator (which is subsequently amplified). We observe that the linewidth reaches a minimum below -15 dBm, indicating that in this regime the linewidth is not power-broadened. Both samples, the natural-abundance material and the ^{15}N-labelled version, show highly similar behavior, demonstrating that the ^{15}N hyperfine interaction is not the dominant factor for the observed ODMR linewidth in iLOV. For the *Cra*Cry sample, higher RF power was required; otherwise, the ODMR signal would have been too weak. For that reason, we used an output power of -10 dBm at the signal source for the comparison measurements shown in the Extended Data Figure 3.

Supplementary Note 7. Transient absorption spectroscopy and pulsed ODMR experiments

It is well known that LOV domains (incl. iLOV) form a triplet state of FMN after photoexcitation[7]. For that reason, we performed transient absorption (TA) experiments to probe the triplet state lifetime for our sample. Extended Data Figure 4a shows the room temperature TA decay of iLOV, probed at 600 nm after 460 nm excitation. A single-exponential fit yields a triplet-state FMN lifetime of ~28 µs. This lifetime is in agreement with results obtained from Kopka et al.[7] and we assign this lifetime to the decay of the ^{3}FMN state accordingly. TA did not provide any direct spectroscopic evidence for a radical pair, suggesting that it might be obscured by the dominant triplet signal or only weakly populated.

The ODMR experiments presented in the main manuscript were performed under continuous (cw) RF and optical excitation (apart from the on/off cycles required for sample recovery). To gain mechanistic insight, we separated the optical excitation from the RF control (pulsed ODMR). This approach provides, for instance, information on how long the spin state can be manipulated after optical excitation. In Extended Data Figure 4b, the excitation laser is pulsed with a fixed 10 µs duration (10% duty cycle compared to the cw-ODMR experiments), while

the RF pulse duration is swept from 2 µs to 100 µs. The laser-RF pulse cycle was iterated continuously over a total camera acquisition period of 100 ms. The reduced duty cycle (i.e. shorter laser exposure and consequently fewer photons per experiment) leads to a reduction in the overall ODMR contrast (see also Supplementary Note 4). The ODMR contrast continues to increase with increasing RF pulse duration, persisting for tens of microseconds after optical excitation—comparable to the lifetime of the FMN triplet state in iLOV. The SCRP lifetime and the spin polarization of the ^{3}FMN state are both very likely much shorter than this time scale. In a simple model where the FMN triplet state decays both to the FMN ground state (e.g., via phosphorescence) and to a SCRP, the overall triplet decay rate is the sum of the two individual rates (k_{GS} + k_{SCRP}). This is the same rate at which the SCRP is formed, namely k_{GS} + k_{SCRP}. Consequently, the FMN triplet state (with a lifetime of tens of microseconds) continuously generates SCRPs throughout its lifetime which is observed in Extended Data Figure 4b.

Supplementary Note 8. Magnetic field calibration with RF sweeping

For the magnetic field imaging shown in Figure 3, we chose to sweep the RF under static magnetic field conditions. This comes with the artifacts induced by the RF dependent lineshape as discussed in Supplementarty Note 2. Figure S8a depicts the iLOV ODMR spectrum at two different magnetic fields: the light green curves correspond to the lower field (44.0 mT), and the dark green curves to the higher field (44.9 mT) with a strong modulation in the lineshape. We found that we can empirically estimate the average resonance frequency using

$$\overline{f} = \frac{\sum_i freq_i \cdot C_i}{\sum_i C_i}$$

where $\overline{f}$ is the average resonance frequency, $freq_i$ is the swept RF and C_i is the ODMR contrast for each RF. The estimated average resonance frequencies are marked by a red star (for the light green data) and a blue star (for the dark green data) in Figure S8b which corresponds very well with the BNNTs resonances (black and grey) at these magnetic fields.

We further investigate the accuracy of average resonance frequency estimation in Fig. S8c. Using five ODMR spectra from iLOV and BNNTs, the average resonance frequency of iLOV was fitted as a linear function of the calibrated magnetic field strength. The resulting slope closely matches the electron gyromagnetic ratio of ~ 28 GHz/T.

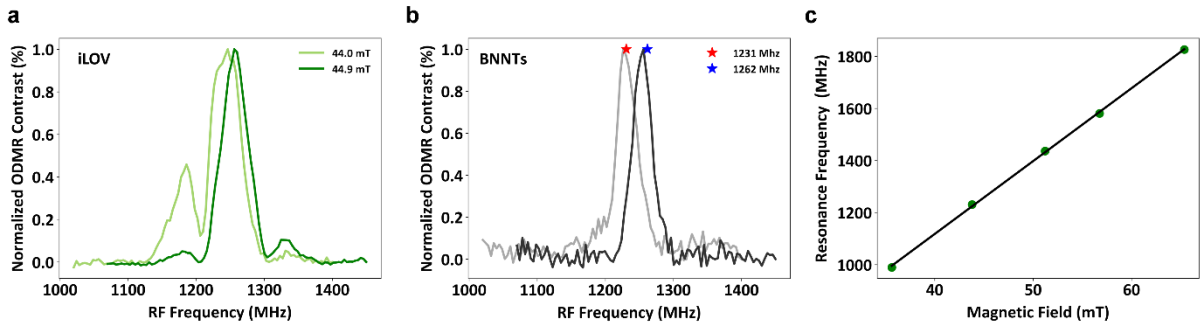

Figure S8. Magnetic field calibration of iLOV for imaging applications. a) and b) ODMR spectra at different magnetic fields of iLOV and BNNTs, respectively. c) Calibration with our empirical model.

Supplementary Note 9. Validation of the magnetic field gradient with BNNTs

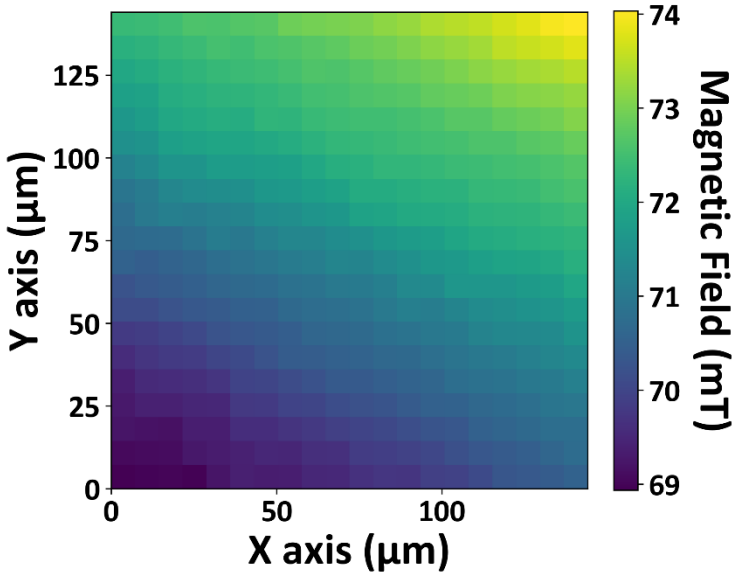

Figure S9. Magnetic field imaging using BNNTs.

To validate the magnetic field map shown in Figure 3b, we used BNNTs homogeneously dispersed on a glass plate as a reference, positioned in the same way as the protein sample. Magnetic field imaging of the BNNTs reveals the overall same spatial gradient (decreasing from the upper right to the lower left) that we observe for the iLOV system. The slightly steeper gradient in the BNNT data may result from the manual positioning of the samples relative to the magnet and the associated differences in their exact placement. Additional deviations may arise from differences in sample geometry: the BNNT sample forms a thin solid film (< 10 µm), whereas the iLOV sample is a ~100 µm-thick liquid layer trapped between cover slides.

We also note that, due to the excitation-dependent ODMR contrast (Supplementary Note 4) of the protein systems, the Gaussian excitation profile of the laser leads to reduced SNR at the corners of the image. This issue can be mitigated in future experiments by shaping the laser beam profile.

References:

1. Kattnig, D. R. *et al.* Chemical amplification of magnetic field effects relevant to avian magnetoreception. *Nat. Chem.* **8**, 384–391 (2016).
2. Déjean, V. *et al.* Detection of magnetic field effects by confocal microscopy. *Chem. Sci.* **11**, 7772–7781 (2020).
3. Berndt, A. *et al.* A Novel Photoreaction Mechanism for the Circadian Blue Light Photoreceptor Drosophila Cryptochrome. *J. Biol. Chem.* **282**, 13011–13021 (2007).
4. Song, S.-H. *et al.* Formation and Function of Flavin Anion Radical in Cryptochrome 1 Blue-Light Photoreceptor of Monarch Butterfly. *J. Biol. Chem.* **282**, 17608–17612 (2007).
5. Rizzato, R. *et al.* Quantum sensing with spin defects in boron nitride nanotubes. *Nat. Commun.* **16**, 11333 (2025).
6. Gao, X. *et al.* Nanotube spin defects for omnidirectional magnetic field sensing. *Nat. Commun.* **15**, 7697 (2024).
7. Kopka, B. *et al.* Electron transfer pathways in a light, oxygen, voltage (LOV) protein devoid of the photoactive cysteine. *Sci. Rep.* **7**, 13346 (2017).